nature communications

Article

https://doi.org/10.1038/s41467-024-55095-z

Anti-aliased metasurfaces beyond the Nyquist limit

Received: 13 August 2024

Accepted: 26 November 2024

Published online: 06 January 2025

Check for updates

Seokwoo Kim[1,6], Joohoon Kim[1,6], Kyungtae Kim[1,6], Minsu Jeong[1] & Junsuk Rho[1,2,3,4,5]

Sampling is a pivotal element in the design of metasurfaces, enabling a broad spectrum of applications. Despite its flexibility, sampling can result in reduced efficiency and unintended diffractions, which are more pronounced at high numerical aperture or shorter wavelengths, e.g. ultraviolet spectrum. Prevailing metasurface research has often relied on the conventional Nyquist sampling theorem to assess sampling appropriateness, however, our findings reveal that the Nyquist criterion is insufficient guidance for sampling in metasurface. Specifically, we find that the performance of a metasurface is significantly correlated to the geometric relationship between the spectrum morphology and sampling lattice. Based on lattice-based diffraction analysis, we demonstrate several anti-aliasing strategies from visible to ultraviolet regimes. These approaches significantly reduce aliasing phenomena occurring in high numerical aperture metasurfaces. Our findings not only deepen the understanding in phase gradient metasurface but also pave the way for high numerical aperture operation down to the ultraviolet spectrum.

Metasurfaces are flat optical components that have drawn substantial attention for their various abilities to control electromagnetic waves. Among these, phase gradient metasurfaces, which manipulate the wavefront of light at a subwavelength scale, stand out due to their versatility[1–3]. Wavefront transformation is achieved by periodically arranged subwavelength scatterers, so-called meta-atoms. They can encode the local phase within each pixel according to the desired phase profile. When incident waves pass through the metasurface, the desired wavefront becomes reconstructed. This sampling-based design principle can be applied to various applications, e.g. lenses[4–6], holograms[7–12], vortex beams[13,14], and structured light[15,16].

However, sampling is a double-edged sword. Despite the flexibility, metasurfaces encoded by high numerical aperture (NA) phase function suffer from fundamental efficiency limits[17,18]. Furthermore, coarse sampling leads to unintended diffractions having distorted momenta[19,20], which can be understood as a wagon-wheel effect in the metasurface (Fig. 1). These issues hinder the metasurface from high NA operation with high signal-to-noise ratio (SNR), which is crucial in extending detection ranges in light detection and ranging (LiDAR) systems[15,16,21], broadening the field of view (FOV) in augmented reality/virtual reality (AR/VR) devices[22,23], and enhancing resolution in imaging and fabrication systems[24,25]. Fine sampling through smaller pixel size can alleviate those challenges, however, it leads to decreased effective index or reduced anisotropy of meta-atoms, which demands a high aspect ratio for full phase modulation, making fabrication more challenging[26,27]. Furthermore, a small area of unit cells limits the degree of freedom in designing meta-atoms having complex topology[28,29]. As the wavelength shortens, especially in the ultraviolet (UV) regime, sampling problems become severe due to the more stringent sampling condition and relatively low refractive index of a lossless dielectric in the UV spectrum[30]. Nevertheless, not only an analysis of distorted

[1]Department of Mechanical Engineering, Pohang University of Science and Technology (POSTECH), Pohang 37673, Republic of Korea. [2]Department of Chemical Engineering, Pohang University of Science and Technology (POSTECH), Pohang 37673, Republic of Korea. [3]Department of Electrical Engineering, Pohang University of Science and Technology (POSTECH), Pohang 37673, Republic of Korea. [4]POSCO-POSTECH-RIST Convergence Research Center for Flat Optics and Metaphotonics, Pohang 37673, Republic of Korea. [5]National Institute of Nanomaterials Technology (NINT), Pohang 37673, Republic of Korea. [6]These authors contributed equally: Seokwoo Kim, Joohoon Kim, Kyungtae Kim. e-mail: jsrho@postech.ac.kr

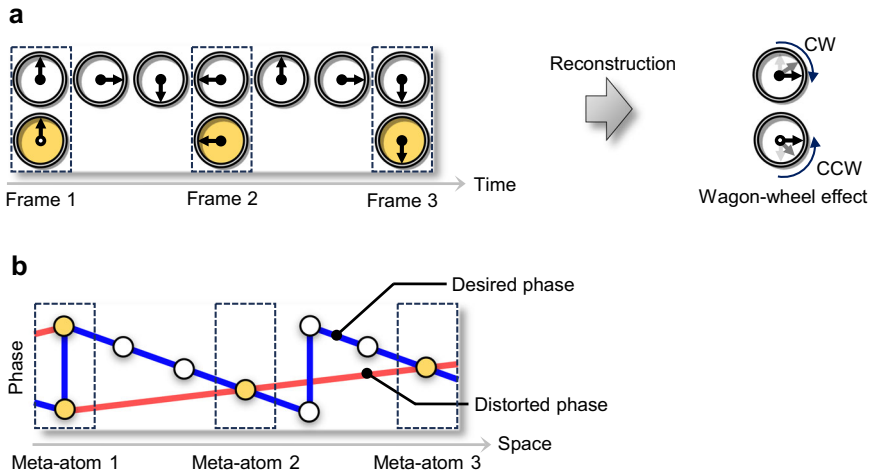

Fig. 1 | The wagon-wheel effect in metasurface. a Schematic illustration of the temporal sampling system. The arrow rotating in a clockwise (CW) direction is captured over a few frames in time, leading observers to perceive it as rotating counterclockwise (CCW) after reconstruction. This visual illusion is commonly referred to as the 'wagon-wheel effect'[43]. **b** Schematic illustration of spatial sampling in a metasurface. The desired phase profile (blue line) is sampled by a few meta-atoms on the metasurface. However, the set of sampled phases (denoted as yellow circles) also can reconstruct another phase profile (red line), which has an opposite sign of slope. This ambiguity leads to the spatial wagon-wheel effect occurring in the metasurface, manifesting as unwanted diffractions having distorted transverse momenta.

diffractions but also the anti-aliasing strategies have yet to be fully studied.

Here, we investigate the aliasing phenomena occurring in metasurfaces. We find that the higher-order spectra encoded in metasurfaces can be outcoupled into free space, manifesting as the wagon-wheel effect in diffraction. Moreover, the Nyquist sampling criterion, which is commonly employed in assessing sampling appropriateness, cannot fully determine the exact condition for avoiding distorted diffraction. Through expanding the diffraction analysis into a two-dimensional spectral space, we find that the geometric relationship between the phase spectrum and lattice structure plays a crucial role in determining the aliasing condition of the metasurface. Based on insights obtained from aliasing analysis, we propose anti-aliasing strategies to eliminate distorted diffraction. These approaches markedly eliminate aliasing phenomena occurring in high NA metasurfaces for visible to near-UV metasurfaces.

Results

Diffraction regimes of metasurface

Before proceeding with our discussion, we will use a momentum unit ($k = 2\pi f$) in the form of spatial frequency (f) multiplied by 2π as a standard unit for describing a spectrum of phase profile. First, we start with the simplest case, a one-dimensional (1D) phase gradient metasurface for monochromatic light ($\lambda = \lambda_0$). The meta-atoms are arranged along the x-axis with a subwavelength interval (Λ) to sample the desired phase profile (Fig. 2a). Discrete sampling of the phase profile reproduces the periodic array of the spatial spectrum with interval $G = 2\pi/\Lambda$ in the momentum space[31]. Among them, the n^{th}-order spectra have shifted momenta by nG for an integer n. When the momentum (k) from higher-order spectra falls within the light cone (i.e. $|k| < k_0$ where $k_0 = 2\pi/\lambda_0$), they can propagate into free space, manifesting as an aliasing of metasurface (Supplementary Note 1). To identify the spectral range where aliasing occurs, we construct the diffraction diagram from repetitive light cones in reciprocal space (Supplementary Note 2). Here, the light-cone array is arranged with interval G in the momentum space (Fig. 2a, b). One can imagine that the light cones become closer together as the shorter wavelength (λ_0) and the wider sampling interval (Λ). Especially, when the parameter λ_0/Λ is under the value of 2, light cones start to overlap each other. For any target momentum to be encoded (k_{meta}) in the desired spectrum, it can be coupled to a higher-order light cone when it belongs to an overlap spectral region (Fig. 2b). It results in the aliasing of the metasurface. The parameter λ_0/Λ thus can be regarded as a sampling level of the metasurface since it determines the spectral range susceptible to distortion.

Here, we consider the 1D metasurface where light cones overlap each other, i.e. $\lambda_0/\Lambda < 2$. Assumes an arbitrary momentum $k_{meta} > 0$ within the desired spectrum (Fig. 2b). Depending on the magnitude of k_{meta}, there are three distinct diffraction scenarios for 1D metasurface:

Aliasing-free (AF) regime - When k_{meta} is in a non-overlap spectral region, i.e. $|k_{meta}| < G - k_0$, only the 0^{th}-order light cone is coupled. Therefore, the ideal order (T_{Ideal}) radiates to the free space whereas the aliasing order ($T_{Aliasing}$) doesn't appear. This aliasing-free spectral region is colored yellow in Fig. 2b. Here, the ideal order is defined as the diffraction order that has a desired spectrum while the aliasing order has a higher-order spectrum.

Weak wagon-wheel effect (WW) regime - If k_{meta} is within the range where light cones overlap but still inside the Brillouin zone (BZ), i.e. $G - k_0 < |k_{meta}| < G/2$, the incident light is coupled to both 0^{th}-order and adjacent higher-order light cones. Different from the AF regime, the coupling of higher-order light cones leads to the outcoupling of aliasing order having the shifted momentum $k_{aliasing} = k_{meta} - G$. The magnitude of imparted transverse momentum of aliasing order is larger than those of ideal order, i.e. $k_{aliasing} > k_{meta}$. Note that the spectrum belonging to the WW regime satisfies the Nyquist criterion since the BZ boundary corresponds to the Nyquist limit ($|k_{meta}| = G/2$), which is defined as half of the sampling frequency in momentum unit (G). This implies that, counterintuitively, the Nyquist criterion cannot ensure unintended diffraction in the free space. This spectral region is colored red in Fig. 2b.

Strong wagon-wheel effect (SW) regime – When k_{meta} lies outside the BZ, i.e. $G/2 < |k_{meta}|$, incident light is coupled to both 0^{th}-order and adjacent higher-order light cones where the transverse momentum of aliasing order is smaller than those of ideal order, i.e. $|k_{meta} - G| = |k_{aliasing}| < |k_{meta}|$. The spectrum belonging to this regime does not satisfy the Nyquist sampling criterion since it is outside of BZ. This spectral region is colored blue in Fig. 2b.

As a proof of concept, the diffraction efficiencies of the beam steering metasurface are calculated for various sampling levels (Fig. 2c–e). The metasurface is targeted for normally incident light with a wavelength of 325 nm. The rigorous coupled-wave analysis (RCWA) is

https://doi.org/10.1038/s41467-024-55095-z

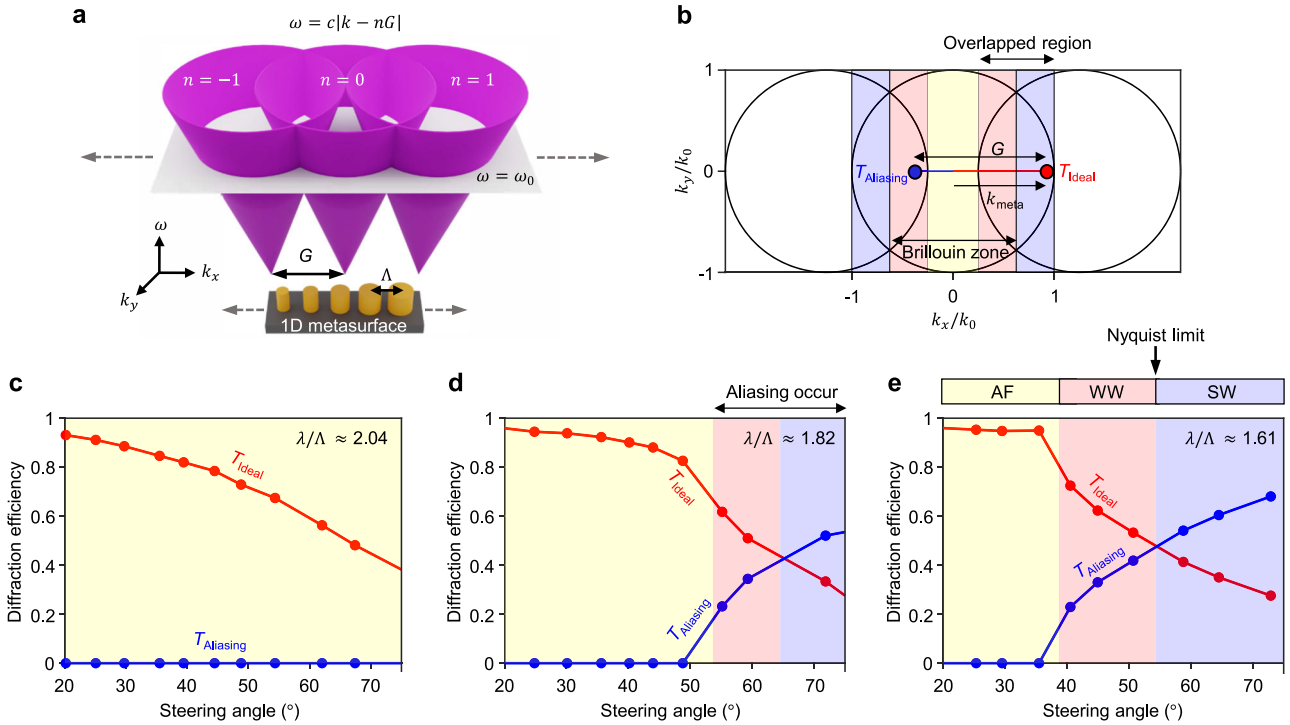

Fig. 2 | Aliasing in 1D beam steering metasurface. a Schematic illustration of 1D metasurface and reproduced light cones in the momentum space. The spectral range where aliasing occurs can be obtained from overlapping light cones. Depending on the target frequency of light (ω_0) and the sampling interval (Λ), the range of overlap spectral region is determined. **b** The cross-section of light cones at the target frequency. Depending on the magnitude of the encoded momentum ($|k_{meta}|$), the normally incident light can couple not only the 0th-order light cone but also the adjacent higher-order light cone. **c**–**e** Calculated diffraction efficiency for various sampling levels where (c) $\lambda/\Lambda = 2.04$, (d) $\lambda/\Lambda = 1.82$, (e) $\lambda/\Lambda = 1.61$, respectively. Yellow, red, and blue colors in the graphs represent the three diffraction regimes, AF, WW, and SW regimes, respectively.

employed to determine diffraction efficiencies of various steering angles (Methods). Different sets of meta-atoms are used for each sampling level whose refractive index is 2, and their height is determined to ensure full phase modulation from 0 to 2π (Supplementary Note 3). The red and blue curves in Fig. 2c–e represent the diffraction efficiency of T_{Ideal} and $T_{Aliasing}$, respectively. Here, we define diffraction efficiency as the ratio of power coupled into each diffraction order to the total transmitted light.

In Fig. 2c–e, T_{Ideal} decreases as the steering angle increases, due to the reduced number of sampled phases since the phase gradient becomes steeper. When the light cones overlap, i.e. the sampling level is under 2, the WW and SW regimes emerge (Fig. 2d, e). At the WW regime, aliasing starts to emerge, and its efficiency increases as the steering angle increases. This is because the magnitude of imparted momentum of aliasing order ($k_{aliasing} = |k_{meta} - G|$) decreases as the desired momentum k_{meta} increases. In the SW regime, the efficiency of the aliasing order eventually surpasses the ideal order. Note that as long as the sampling level of the metasurface remains unchanged, the ideal and aliasing order cannot be decoupled from each other (Supplementary Note 4). The sampled surface profile obtained by k_{meta} inherently includes the sampling of $k_{aliasing}$. In other words, an observer cannot distinguish whether the surface profile was generated by sampling k_{meta} or $k_{aliasing}$.

For instance, if k_{meta} is coarsely sampled, this results in two diffraction channels, T_{Ideal} and $T_{Aliasing}$. Here, T_{Ideal} will carry the transverse momentum of k_{meta}, while $T_{Aliasing}$ will carry the transverse momentum of $k_{aliasing}$. Conversely, if $k_{aliasing}$ is sampled, $T_{Aliasing}$ becomes the desired order, and the aliasing channel would then be represented by T_{Ideal}. This demonstrates that the aliasing channel is not merely an independent, unwanted diffraction channel but rather considered as an ideal diffraction channel with a different transverse momentum. Therefore, efforts to enhance the diffraction efficiency of T_{Ideal}—such as by increasing the transmittance of the meta-atom or enhancing the conversion efficiency of PB-meta-atom—will inevitably lead to an increase in the efficiency of $T_{Aliasing}$, provided the sampling level remains unchanged.

Anisotropic performance of sampling lattice

Now, the aliasing analysis is further extended to a metasurface composed of a two-dimensional (2D) lattice, which is a more general case (Supplementary Note 5). While square lattice and hexagonal lattice are commonly employed in metasurfaces, it is possible to generate an arbitrary sampling lattice using two nonparallel vectors[31]. Akin to a previous 1D case, we can construct a diffraction diagram for identifying diffraction regimes from the array of light cones positioned at each point generated by the linear combination of the reciprocal basis vectors (Fig. 3a, b). For instance, Fig. 3c presents the diffraction diagram for a square lattice at a sampling level of 1.58, where yellow, red, and blue colored spectral regions in the diagram represent AF, WW, and SW diffraction regimes, respectively.

Consider the scenario where arbitrary momentum $\vec{k}_{meta}$ is imparted to incident light through this sampling lattice. Here, NA for $\vec{k}_{meta}$, i.e. $|\vec{k}_{meta}|/k_0$, is assumed to be 0.82, which is represented by the red dashed circle (Fig. 3c). Although its sampling lattice doesn't satisfy the Nyquist criterion ($|\vec{k}_{meta}|/k_0 > \lambda_0/2\Lambda = 0.79$), interestingly, one can observe that the diffraction regimes vary depending on the azimuthal direction of $\vec{k}_{meta}$. Specifically, if the direction of the momentum is parallel to the lattice vectors, along the x or y-axis, then the momentum falls into the SW region, however, if the momentum's direction is diagonal, the spectrum then belongs to the AF regime (Fig. 3c). This observation implies that each sampling lattice has specific directions that are particularly advantages for large-angle

https://doi.org/10.1038/s41467-024-55095-z

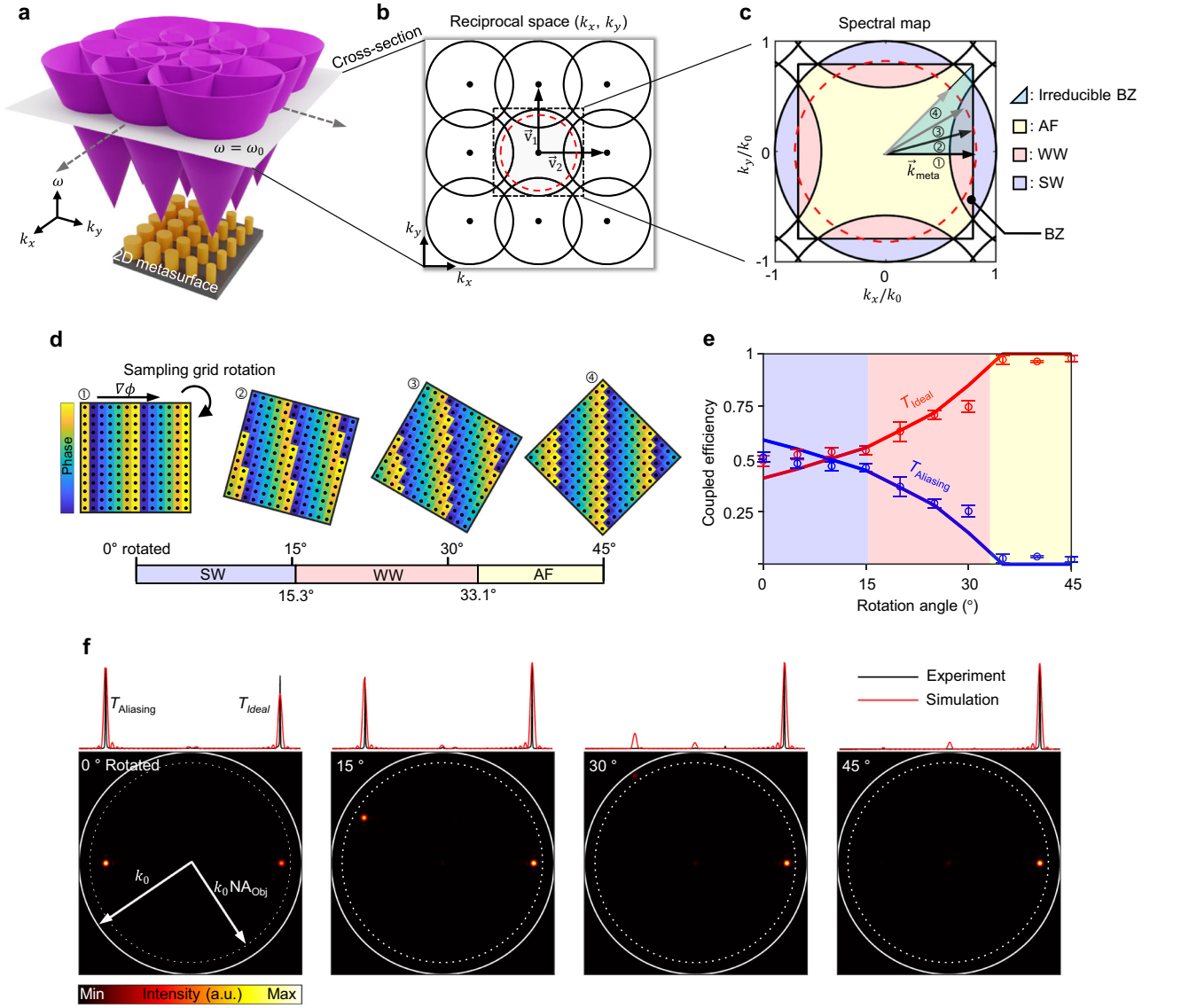

Fig. 3 | Anti-aliasing of metasurface by rotating sampling lattice. a Schematics of a metasurface and its corresponding light cone array in the momentum space. **b** Cross-section of the light cones at the target frequency ($\omega = \omega_0$). **c** Diffraction diagram obtained from overlap light cones, identifying different diffraction regimes. The regimes of AF, WW, and SW are indicated in yellow, red, and blue, respectively. **d** Illustration of rotated sampling lattices with an identical phase map, highlighting how diffraction regimes change in terms of the rotation angle of the sampling lattice. **e** The efficiency ratio between ideal and aliasing order as a function of the sampling lattice's rotation angle. The measurements were repeated 5 times; error bars represent the standard deviation. The solid line represents calculated data from finite-difference time-domain (FDTD) simulation. **f** Presentation of experimental (black line) and calculated (red line) far-field radiation pattern (top). The momentum space images (bottom) are calculated from FDTD simulation. The outer and inner dotted circles in the momentum space image represent the light cone and the NA of the objective lens, respectively.

diffraction, which is not observed phenomenon in the 1D sampling case. Moreover, simply aligning the superior direction of the sampling lattice with that of the directional spectrum can serve as an effective anti-aliasing strategy.

As a proof of concept, we experimentally demonstrate the Pancharatnam-Berry metasurface[1,32] designed for steering light at an angle of 55°, which corresponds to the NA of about 0.82. The metasurface is designed based on a square lattice with a periodicity of 400 nm, targeting a wavelength of 632 nm, which corresponds to a sampling level of 1.58. For the meta-atoms, hydrogenated amorphous silicon (a-Si:H) is employed, with a refractive index of 2.42 at the target wavelength (Methods and Supplementary Note 6). To validate the anisotropic performance of the metasurface, we fabricate ten different metasurfaces with identical phase profiles, but different sampling grids rotated from 0° to 45° with 5° intervals (Fig. 3d and scanning electron microscope (SEM) images are in Supplementary Note 7). Note that the metasurfaces don't satisfy the Nyquist criterion ($NA > \lambda_0/2\Lambda = 0.79$). Figure 3e shows the efficiency ratio between the ideal and aliasing diffraction order measured by a power meter. Blue, red, and yellow colors denote the diffraction regimes obtained from the diffraction diagram represented in Fig. 3c. When the rotation angle is below about 15°, the diffraction belongs to the SW regime where the efficiency of aliasing slightly surpasses those of ideal order. When the rotation angle exceeds approximately 33°, aliasing nearly disappears even though the periodicity of the lattice doesn't meet the Nyquist criterion. Figure 3f shows the measured momentum space images compared with simulated results (measurement setup is in Supplementary Note 8). One can find that while the direction of the ideal order is invariant due to the identical phase profile for metasurfaces, the aliasing order moves toward the outer edge of the light cone as the

https://doi.org/10.1038/s41467-024-55095-z

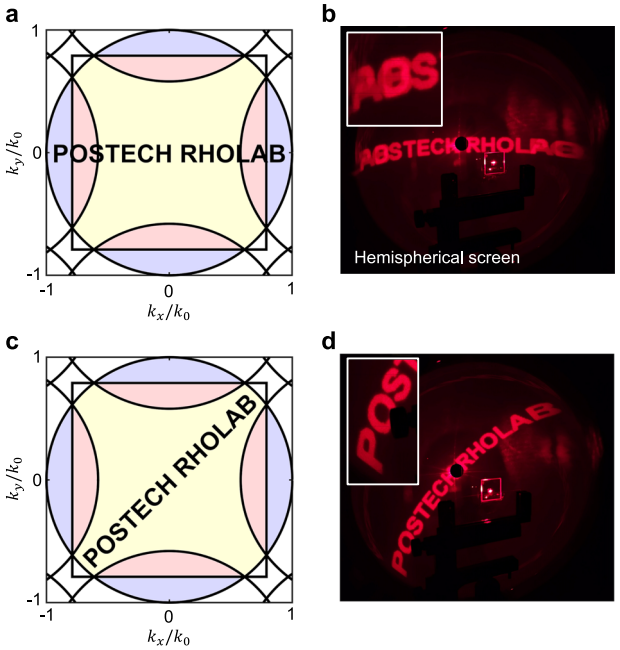

Fig. 4 | Anti-aliasing for wide field of view (FOV) meta-hologram. a, b Spectrum of hologram aligns with the *x*-axis. **c**, **d** Spectrum of hologram is rotated by 45° from the *x*-axis. **a**, **c** Diffraction diagram for the meta-hologram with a maximum NA of 0.94. **b**, **d** Measured wide FOV (FOV of hologram is about 140.2°) hologram images.

rotation angle increases. It is because the transverse momentum of the aliasing order, which can be calculated as $\vec{k}_{\text{meta}} - \vec{\mathbf{v}}_2$, varies according to the grid rotation angle since lattice rotation changes the lattice vector $\vec{\mathbf{v}}_2$. At rotation angles above 25°, the aliasing order moves beyond the NA of the objective lens (0.9) and is no longer observable (Supplementary Note 9).

To further demonstrate the versatility of the anti-aliasing method through lattice rotation, we extended its application to wide FOV holograms (Fig. 4). The set of meta-atoms composing the metasurface is the same as that used for beam steering. Note that the maximum NA of the hologram is 0.94 (the FOV of a hologram is about 140.2°), exceeding the Nyquist limit NA of 0.79. We fabricate two metasurfaces with the lattice of the square grid aligned at 0° and 45° relative to the hologram spectrum. In the aliasing map for the 0° alignment, the letters 'P' and 'B' fall into the SW region, while the letters 'O', 'S', 'L', and 'A' are partially in the WW region (Fig. 4a). In contrast, when rotated by 45°, all letters fall into the AF region (Fig. 4c). We fabricate metasurfaces for both cases and measure the hologram (see Fig. 4b and d, and measurement setup is in Supplementary Note 10). As expected, when the spectrum is rotated by 45°, aliasing is effectively suppressed, even at high-NA region (see inset boxes for Fig. 4b and d). In Fig. 4b, the letters 'P' and 'O' are overlapped with the aliasing order of the letters 'A' and 'B', however, there is no aliasing observed in Fig. 4d (Supplementary Video 1).

Lattice-dependent characteristics in metalens

Now we investigate the effect of sampling lattice in a metalens, which is one of the prominent applications for phase-gradient metasurfaces. Unlike the directional momentum encoded for beam steering, the spectrum for beam focusing is isotropic for all azimuthal directions. In addition, for a high NA metalens, the spectrum nearly spans the entire cross-section of a light cone. Consequently, high NA metalenses can exhibit varying diffraction regimes depending on the radial distance from the center. For example, for the high NA metalens having a low sampling level, aliasing can prevail at the edge of the metalens. Thus, the light transmitted through the high NA metalens mostly coupled to the focusing ideal orders, diverging aliasing orders, and non-diffracted zeroth orders (Fig. 5a).

Figure 5b presents a diffraction diagram for a hexagonal lattice and a square lattice. Although two lattices have an identical sampling level (1.26), they exhibit distinct shapes and areas for diffraction regimes (Supplementary Note 11). The range of NA of metalens for avoiding the SW regime, i.e. the Nyquist criterion, becomes $\text{NA} < \frac{\lambda}{\sqrt{3}\Lambda} \approx 0.58\frac{\lambda}{\Lambda}$ for a hexagonal lattice. In contrast, the coefficient on the right-hand side of the equality becomes 0.5 for the square lattice case, indicating a more stringent condition compared to a hexagonal lattice (Supplementary Note 12).

As a proof of concept, we fabricate the hexagonal lattice and square lattice metalenses for NA of 0.99 and 0.65, respectively (Methods and SEM images are in Supplementary Note 13). All metalens are based on a hyperbolic phase profile and have the same periodicity (500 nm), a target wavelength (632 nm), and a sampling level of 1.26. Note that the periodicity of the metasurface is set to be much more relaxed than the capability limit of E-beam lithography, intentionally allowing us to observe how aliasing occurs on the metalens. The meta-atom table for the square lattice and hexagonal lattice is in Supplementary Note 14. Figure 5c–f shows the light intensity distribution after passing through the metalenses for NA of 0.99 and 0.65, respectively (measurement setup is in Supplementary Note 15). Metalenses sampled on different lattices show distinct diffraction patterns, particularly associated with aliasing radiating outward to the optical axis. When NA approaches unity, the spectrum spans the almost entire light cone so that clear aliasing patterns are observed (Fig. 5c, d and Supplementary Video 2). The calculated focusing efficiencies for the hexagonal and square lattice metalens (NA = 0.65) are 49.3% and 40.2%, respectively, where the focusing efficiency is calculated as the ratio of incoming power in the circle encircling with a radius of 3 times full-width half maximum of PSF to the input power. The total quantity of the sum of unwanted diffraction and non-diffracted 0^{th} order for two different lattice metalenses, which can be obtained as the difference between the transmittance and the focusing efficiency, is 18.4% and 26.3%, respectively. When NA is 0.65, almost no aliasing is observed in hexagonal lattice metalens (Fig. 5e), whereas the square lattice metalens exhibit aliasing channels radiating to four orthogonal directions due to coupling with adjacent light cones (Fig. 5f). The diffraction diagram in Fig. 5b reveals the existence of partial spectra coupling with the adjacent light cones even in hexagonal lattice metalens, but these are nearly unobserved since the NA of the objective lens used in measurements limits the observable spectrum in the momentum space (Supplementary Note 16).

Anti-aliasing by integrated lattice

The resolution of standard lithography techniques constrains the feasible dimensions for unit cells of metasurface. Consequently, the sampling level of a metasurface inevitably decreases with a shorter wavelength, leading to more pronounced sampling-induced issues in the UV spectrum application. To mitigate this, we counteract aliasing phenomena in the high NA (0.9) metalens targeted for near-UV light (405 nm), by integrating an array of meta-dimers on the periphery of the metalens (Fig. 6d). Although heterogeneous designs of metalenses, where metasurfaces are combined with grating structures, have been proposed in recent years[24,33–36], the anti-aliasing aspect, particularly in short wavelength regimes, remains underexplored. It should be noted that the reason we demonstrated the anti-aliasing at a 405 nm wavelength is not due to an inability to implement it at shorter wavelengths, but rather because commercial high-NA objective lenses for precise characterization, such as PSF and aliasing pattern spreading with high NA angle, are rarely available in the UV wavelength range (Demonstrations at shorter wavelength of 320 nm and 255 nm are in Supplementary Note 17).

https://doi.org/10.1038/s41467-024-55095-z

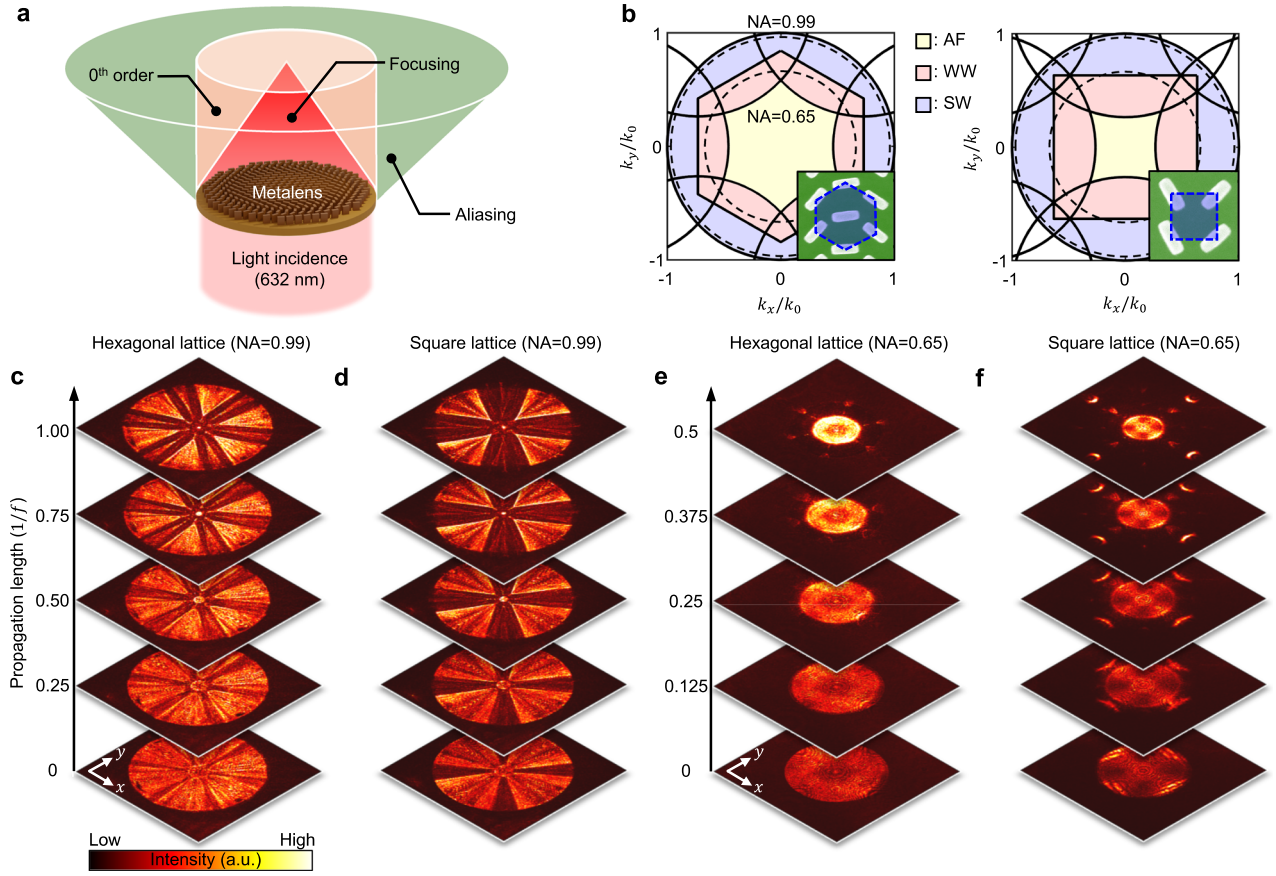

Fig. 5 | Aliasing in metalens. a The three dominant diffraction channels in high NA metalens. **b** Diffraction diagrams in a hexagonal lattice (left) and square lattice (right) and SEM image of the fabricated metalens (insets). The inner and outer dotted circles represent the spectral boundary having NA 0.99 and 0.65. **c, d** The measured intensity distribution of diffracted light after transmitting (**c**) the hexagonal lattice and (**d**) square lattice metalens with an NA of 0.99. **e, f** The measured intensity distribution of diffracted light after transmitting (**e**) the hexagonal lattice and (**f**) square lattice metalens with an NA of 0.65.

The meta-atom table for near-UV metalens is in Supplementary Note 18. Each meta-dimer consists of two closely located nanostructures (Fig. 6a). The small intervening gap facilitates non-local coupling between two vertical waveguides. This coupling results in directional energy flows[37] (its time-averaged Poynting vector representation is depicted in Fig. 6b) within the meta-dimer. This resulted from the 'beating effect' that is interference between several coupled guided modes, rendering it more effective for large-angle scattering compared to conventional sampling-based metasurfaces[24,37–39].

The integration of meta-dimers has been optimized for various steering angles using RCWA (Supplementary Note 19). Notably, the diffraction efficiency of the meta-dimer array exceeds that of conventional metasurfaces at an angle of approximately 24° (Supplementary Note 20). Beyond this transition angle, we combine the meta-dimer array with the hexagonal lattice metalens, taking into account the phase of light diffracted after transmission through the meta-dimers, as shown in Fig. 6d. The meta-dimer array is strategically positioned along the peripheries of concentric circles, with each circle's radius tailored to align the meta-dimers' phase with the hexagonal lattice metalens' phase profile. It is crucial to achieve coherent alignment, as the light scattered from both the meta-dimer and meta-atom arrays must constructively converge at the focal point (Supplementary Note 21).

In Fig. 6c, the hatched area in the diffraction diagram represents the spectrum where meta-dimers are integrated, which includes all overlap spectral regions where aliasing occurs. In this regard, the replacement of a high NA part with a meta-dimer array can significantly reduce the distorted diffraction. As a proof of concept, we fabricate two conventional metalens based on a square lattice and hexagonal lattice and anti-aliased metalens based on the integrated lattice (Methods and SEM images are in Supplementary Note 22). Figure 6e, f illustrates the measured intensity profiles at the focal plane for both integrated lattice metalens and conventional metalens (measurement setup is in Supplementary Note 23). The aliasing radiating outward from the optical axis is substantially reduced in the integrated lattice metalens (Supplementary Note 24 and Supplementary Video 3). Moreover, the measured peak intensity at the focal plane for the integrated lattice metalens is about twice higher than that of other hexagonal and square metalenses (Supplementary Note 25). The measured (simulated) focusing efficiency of the integrated lattice metalens is around 48.5% (57.8%), while the focusing efficiencies of the hexagonal and square lattice metalenses are significantly lower, at approximately 21.3% (28.6%) and 19.8% (25.4%), respectively. Here, the focusing efficiencies are measured based on the total flux of the aperture at the focal plane where the aliased diffractions are not counted (Supplementary Note 26). The radius of the aperture is set to 0.05 times the diameter of the metalens. Although the undiffracted light can enter the aperture, its effect is negligible since the aperture area accounts for only 1% of the total lens area. And the aliasing channel is also barely counted within the aperture (see Supplementary Note 24).

Discussion

In this study, we analyze aliasing in metasurfaces and develop effective anti-aliasing strategies. We discover that inadequate sampling leads to the outcoupling of higher-order spectra into the

https://doi.org/10.1038/s41467-024-55095-z

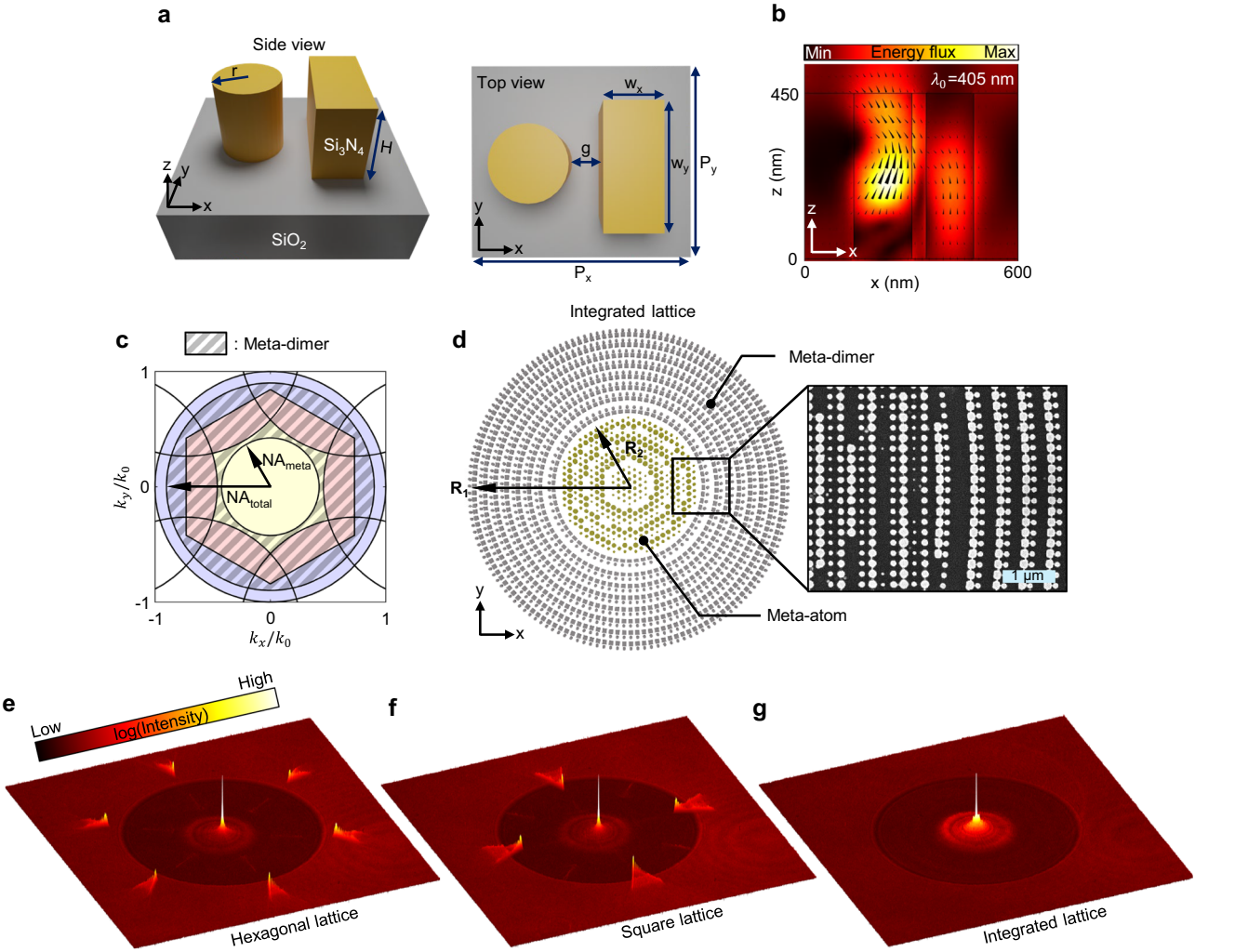

Fig. 6 | Anti-aliasing metalens via integration of meta-dimer. a Schematic of meta-dimer consists of two coupled vertical waveguides. **b** Calculated time-averaged Poynting vector in *xz*-plane of meta-dimer. **c** Diffraction diagram of hexagonal metalens. Hatched area represents the spectrum where meta-dimers are integrated, including all the spectrum where aliasing occurs. **d** Schematic illustration of meta-dimer integrated metalens and SEM image of the fabricated UV metalens. **e, f, g** Intensity distribution at the focal plane for (**e**) hexagonal lattice metalens, (**f**) square lattice metalens, and (**g**) meta-dimer integrated metalens.

free space, manifesting as aliasing radiating in distorted directions. We find that the commonly employed Nyquist sampling criterion cannot prevent unintended diffraction. Moreover, we suggest that achieving aliasing-free reconstruction by a metasurface is not solely determined by its sampling periodicity; It requires a comprehensive understanding of the geometric interplay between the spectrum morphology and the sampling lattice structure. Table 1 summarizes the key findings of our research. Note that this is still valid for immersion oil applications where refractive index of output medium is nonzero ($n_{out}\neq1$).

This insight leads to the development of anti-aliasing strategies for metasurfaces. For beam steering metasurfaces with directional spectra and wide FOV meta-holograms with anisotropic spectra, the rotation of the sampling lattice effectively eliminates aliasing by disrupting the coupling between the spectrum and higher-order light cones. In metalenses represented by isotropic spectra, the selection of the proper sampling lattice or coherent integration of optimized scatterers can significantly reduce aliasing phenomena. Combining with inverse design enables more efficient exploration of super-pixel geometries, considering the stitching error or fabrication constraints, achieving high-efficiency metasurface applications[35,36,39].

Anti-aliasing can not only eliminate undesired diffractions but also allow for larger unit cell sizes, which enables the complex design of meta-atoms[29,40,41] or relaxation of fabrication constraints. Additionally, the diffraction diagram obtained from light cone arrays helps identify the most effective diffractive direction for a given sampling lattice, in terms of both aliasing and efficiency. Therefore, based on the morphology of the desired spectrum, we can select a more effective sampling lattice. Additionally, exploring other sampling lattices, such as periodic Bravais lattices, quasi-periodic lattices, or even random lattices, which are not covered in this study, can be a very intriguing topic.

In conclusion, the aliasing in metasurface has been largely overlooked during rapid advancements in the field of metasurface. It is noted that aliasing should be regarded as a distinct issue, separated from the efficiency reduction of the desired diffraction. Aliasing that radiates unintended directions can serve as a non-negligible noise in optical devices. We emphasize that our findings are not limited to steering or focusing; they can be applied to the whole spectrum of metasurfaces, including various holograms, structured beams, and other multi-functional wavefronts. With a deeper understanding of metasurface, we envision that our research paves the way for advanced high NA operation even in UV light.

Table 1 | The aliasing-free condition for the metasurface

Aliasing-free condition in the metasurface	Previous research	The Nyquist sampling criterion			
	Our work	When $G > 2n_{out}k_0$	The Nyquist sampling criterion		
		When $G < 2n_{out}k_0$ (Light cones overlapped)	1D periodic lattice	$\lvert k_{meta}\rvert < G - n_{out}k_0$	
			2D Bravais lattice	Isotropic spectrum (e.g., lens, axicon)	$\lvert \boldsymbol{k}_{meta}\rvert < \min(\lvert \boldsymbol{G}_1\rvert, \lvert \boldsymbol{G}_2\rvert) - n_{out}k_0$ where $\boldsymbol{G}_1$ and $\boldsymbol{G}_2$ are reciprocal vectors for the Bravais lattice.
				Anisotropic spectrum (e.g., beam steering, hologram)	It can be a more stringent or relaxed condition compared to the Nyquist criterion, depending on the geometric relationship between the sampling lattice and the spectrum morphology.

Here, k_{meta} is the momentum to be sampled in the metasurface, $G = 2\pi/\Lambda$ is from the sampling periodicity (Λ) of metasurface, n_{out} is the refractive index of output medium, and k_0 is the wavevector of incident light.

Methods

Metasurface fabrication

Beam steering metasurface, visible metalens, and UV metalens were fabricated on a 500-μm-thick silica substrate.

For the beam steering metasurface, holography metasurface, and visible metalens, an 700-nm-thick a-Si:H was deposited using plasma enhanced chemical vapor deposition (PECVD, BMR Technology HiDep-SC) with a flow rate of 10 sccm for SiH_4 and 75 sccm for H_2. Chamber pressure and operating temperature were 20 mTorr and 200 °C, respectively. Metasurfaces were transferred onto the positive photoresist (Microchem, 495 PMMA A2) by using a standard electron beam lithography process (ELINOIX, ELS-7800, acceleration voltage: 80 kV, beam current: 100 pA). Then, a 50-nm-thick chromium layer was deposited using electron beam evaporation (KVT, KVE-ENS4004). A lift-off process was proceeded and residual chromium patterns were used as a hard mask for the a-Si:H etching. After a dry etching process (DMS, silicon-metal hybrid etcher), the remaining chromium was removed using chromium etchant.

For the UV metalens, a 450-nm-thick silicon nitride was deposited using plasma-enhanced chemical vapor deposition (PECVD, BMR Technology HiDep-SC) with a flow rate of 35 sccm for SiH_4 and 35 sccm for H_2. Chamber pressure and operating temperature were 60 mTorr and 300 °C, respectively. Metasurfaces were transferred onto the positive photoresist (ZEON, ZEP520A) by using a high-speed electron beam lithography process (ELINOIX, ELS-BODEN 50H, acceleration voltage: 50 kV, beam current: 1 nA). Then, 50-nm-thick aluminum layer was deposited using electron beam evaporation (KVT, KVE-ENS4004). A lift-off process was proceeded and residual aluminum patterns were used as a hard mask for the silicon nitride etching. After a dry etching process (DRM85DD, TEL), the remaining aluminum was removed using aluminum etchant.

Calculating the diffraction efficiency of metasurface with the rigorous coupled-wave analysis

We calculated the diffraction efficiency of a metasurface by the rigorous coupled-wave analysis (RCWA) method. Typically, metasurfaces are aperiodic, rendering the RCWA method unsuitable. However, if the number of samplings (N) within a projected period is a rational number, i.e. $N \times a = b$ for $a, b \in \mathbb{Z}$, the meta-atom array becomes periodic for the direction parallel to the phase gradient with the periodicity of $b\Lambda$. Here, N can be represented as $\frac{\lambda}{\sin\theta \cdot \Lambda}$ where λ is the wavelength of the incident light, θ is the deflection angle, and Λ is the period of meta-atom. $\lambda/\sin(\theta)$ can be understood as the projected period so that the imparted momentums by ideal and aliasing order are $k_{ideal} = \frac{2\pi}{N\Lambda} = \frac{2\pi a}{b\Lambda}$ and $k_{aliasing} = k_{ideal} - G = \frac{2\pi(a-b)}{b\Lambda}$, respectively. The ideal and aliasing order of the metasurface can be defined as a^{th} and $(a-b)^{th}$ diffraction order in the meta-atom supercell. For example, suppose a metasurface with the number of samplings as $N = 1.75$ for which the integers are $a = 4$ and $b = 7$. The ideal and aliasing order correspond to the 4^{th} and 3^{rd} diffraction order for respectively where the periodicity for supercell is 7Λ. Additionally, to account for the various meta-atom combinations within the super-periodicity, we calculate a set of diffraction efficiencies by varying the phase shift added to the phase profile and take the averaged efficiency as a representative value[42].

Calculating the beam steering efficiency of metasurface

In our study, the simulation of the metalens was conducted utilizing the three-dimensional Finite Difference Time Domain (FDTD) method, as implemented by Lumerical Inc. To ensure accuracy and minimize reflections, Perfectly Matched Layer (PML) boundary conditions were applied along all three axes. Our approach involved a full-wave simulation of the metalens, distinctively omitting the utilization of far-field propagation techniques. The diameter of metalens used for calculation is 25 μm, considering the computational cost.

Data availability

The data that support the findings of this study are available from the corresponding author upon request.

References

1. Lin, D., Fan, P., Hasman, E. & Brongersma, M. L. Dielectric gradient metasurface optical elements. *Science* **345**, 298–302 (2014).
2. Yin, X., Ye, Z., Rho, J., Wang, Y. & Zhang, X. Photonic spin Hall effect at metasurfaces. *Science* **339**, 1405–1407 (2013).
3. Huang, L. et al. Three-dimensional optical holography using a plasmonic metasurface. *Nat. Commun.* **4**, 2808 (2013).
4. Khorasaninejad, M. et al. Metalenses at visible wavelengths: Diffraction-limited focusing and subwavelength resolution imaging. *Science* **352**, 1190–1194 (2016).
5. Zhou, Y., Zheng, H., Kravchenko, I. I. & Valentine, J. Flat optics for image differentiation. *Nat. Photon.* **14**, 316–323 (2020).
6. Kim, J. et al. Scalable manufacturing of high-index atomic layer–polymer hybrid metasurfaces for metaphotonics in the visible. *Nat. Mater.* **22**, 474–481 (2023).
7. Fang, X., Ren, H. & Gu, M. Orbital angular momentum holography for high-security encryption. *Nat. Photon.* **14**, 102–108 (2020).
8. Song, Q., Odeh, M., Zúñiga-Pérez, J., Kanté, B. & Genevet, P. Plasmonic topological metasurface by encircling an exceptional point. *Science* **373**, 1133–1137 (2021).

9. Kim, J. et al. Photonic encryption platform via dual-band vectorial metaholograms in the ultraviolet and visible. *ACS Nano* **16**, 3546–3553 (2022).
10. Kim, J. et al. One-step printable platform for high-efficiency metasurfaces down to the deep-ultraviolet region. *Light Sci. Appl.* **12**, 68 (2023).
11. So, S. et al. Multicolor and 3D Holography generated by inverse-designed single-cell metasurfaces. *Adv. Mater.* **35**, 2208520 (2023).
12. Kim, J. et al. Dynamic hyperspectral holography enabled by inverse-designed metasurfaces with oblique helicoidal cholesterics. *Adv. Mater.* **36**, 2311785 (2024).
13. Wang, B. et al. Generating optical vortex beams by momentum-space polarization vortices centred at bound states in the continuum. *Nat. Photon.* **14**, 623–628 (2020).
14. Mehmood, M. Q. et al. Visible-frequency metasurface for structuring and spatially multiplexing optical vortices. *Adv. Mater.* **28**, 2533–2539 (2016).
15. Juliano Martins, R. et al. Metasurface-enhanced light detection and ranging technology. *Nat. Commun.* **13**, 5724 (2022).
16. Kim, G. et al. Metasurface-driven full-space structured light for three-dimensional imaging. *Nat. Commun.* **13**, 5920 (2022).
17. Swanson, G. J. *Binary optics technology: theoretical limits on the diffraction efficiency of multilevel diffractive optical elements*. (1991).
18. Chung, H. & Miller, O. D. High-NA achromatic metalenses by inverse design. *Opt. Express* **28**, 6945–6965 (2020).
19. Menon, R. & Sensale-Rodriguez, B. Inconsistencies of metalens performance and comparison with conventional diffractive optics. *Nat. Photon.* **17**, 923–924 (2023).
20. Kamali, S. M., Arbabi, E., Arbabi, A. & Faraon, A. A review of dielectric optical metasurfaces for wavefront control. *Nanophotonics* **7**, 1041–1068 (2018).
21. Park, J. et al. All-solid-state spatial light modulator with independent phase and amplitude control for three-dimensional LiDAR applications. *Nat. Nanotechnol.* **16**, 69–76 (2021).
22. Lee, G.-Y. et al. Metasurface eyepiece for augmented reality. *Nat. Commun.* **9**, 4562 (2018).
23. Li, Z. et al. Inverse design enables large-scale high-performance meta-optics reshaping virtual reality. *Nat. Commun.* **13**, 2409 (2022).
24. Paniagua-Domínguez, R. et al. A metalens with a near-unity numerical aperture. *Nano Lett.* **18**, 2124–2132 (2018).
25. Liang, H. et al. Ultrahigh numerical aperture metalens at visible wavelengths. *Nano Lett.* **18**, 4460–4466 (2018).
26. Khorasaninejad, M. & Capasso, F. Metalenses: Versatile multifunctional photonic components. *Science* **358**, eaam8100 (2017).
27. Ndao, A. et al. Octave bandwidth photonic fishnet-achromatic-metalens. *Nat. Commun.* **11**, 3205 (2020).
28. Shi, T. et al. Planar chiral metasurfaces with maximal and tunable chiroptical response driven by bound states in the continuum. *Nat. Commun.* **13**, 4111 (2022).
29. Chen, W. T. et al. A broadband achromatic metalens for focusing and imaging in the visible. *Nat. Nanotechnol.* **13**, 220–226 (2018).
30. Yang, Y. et al. Revisiting optical material platforms for efficient linear and nonlinear dielectric metasurfaces in the ultraviolet, visible, and infrared. *ACS Photonics* **10**, 307–321 (2023).
31. Petersen, D. P. & Middleton, D. Sampling and reconstruction of wave-number-limited functions in N-dimensional euclidean spaces. *Inf. Control* **5**, 279–323 (1962).
32. Zheng, G. et al. Metasurface holograms reaching 80% efficiency. *Nat. Nanotechnol.* **10**, 308–312 (2015).
33. Zhang, J. et al. Metalenses with polarization-insensitive adaptive nano-antennas. *Laser Photonics Rev.* **16**, 2200268 (2022).
34. Byrnes, S. J., Lenef, A., Aieta, F. & Capasso, F. Designing large, high-efficiency, high-numerical-aperture, transmissive meta-lenses for visible light. *Opt. Express* **24**, 5110–5124 (2016).
35. Phan, T. et al. High-efficiency, large-area, topology-optimized metasurfaces. *Light Sci. Appl.* **8**, 48 (2019).
36. Zhou, Y. et al. Large-area, high-numerical-aperture, freeform metasurfaces. *Laser Photonics Rev.* **18**, 2300988 (2024).
37. Patri, A., Kéna-Cohen, S. & Caloz, C. Large-angle, broadband, and multifunctional directive waveguide scatterer gratings. *ACS Photonics* **6**, 3298–3305 (2019).
38. Khaidarov, E. et al. Asymmetric nanoantennas for ultrahigh angle broadband visible light bending. *Nano Lett.* **17**, 6267–6272 (2017).
39. Sell, D., Yang, J., Doshay, S., Yang, R. & Fan, J. A. Large-angle, multifunctional metagratings based on freeform multimode geometries. *Nano Lett.* **17**, 3752–3757 (2017).
40. Liu, Z. et al. High-Q quasibound states in the continuum for nonlinear metasurfaces. *Phys. Rev. Lett.* **123**, 253901 (2019).
41. An, S. et al. Multifunctional metasurface design with a generative adversarial network. *Adv. Opt. Mater.* **9**, 2001433 (2021).
42. Arbabi, A. et al. Increasing efficiency of high numerical aperture metasurfaces using the grating averaging technique. *Sci. Rep.* **10**, 7124 (2020).
43. Purves, D., Paydarfar, J. A. & Andrews, T. J. The wagon wheel illusion in movies and reality. *Proc. Natl Acad. Sci. USA* **93**, 3693–3697 (1996).

Acknowledgements

This work was financially supported by the POSCO-POSTECH-RIST Convergence Research Center program funded by POSCO, an industry-academic strategic grant (IO230728-06857-01) funded by Samsung Electronics, and the National Research Foundation (NRF) grant (RS-2024-00356928) funded by the Ministry of Science and ICT (MSIT) of the Korean government. J.K. acknowledges the Asan Foundation Biomedical Science fellowship, and the Presidential Science fellowship funded by the MSIT of the Korean government. M.J. acknowledges the Hyundai Motor *Chung Mong-Koo* fellowship. The authors thank Dr. Eunpa Kim (Samsung Electronics) for discussions.

Author contributions

J.R. and S.K. conceived the idea and initiated the project. S.K., J.K. and J.R. designed the whole experiments. S.K. and K.K. performed the theoretical studies and numerical simulations. J.K. fabricated the devices. S.K., J.K., K.K. and M.J. performed the experimental characterizations and data analyses. S.K. mainly wrote the paper. All authors parcitipated in discussions and approved the final version of the paper. J.R. guided the entire work.

Competing interests

The authors declare no competing interests.

Additional information

Supplementary information The online version contains supplementary material available at https://doi.org/10.1038/s41467-024-55095-z.

Correspondence and requests for materials should be addressed to Junsuk Rho.

Peer review information *Nature Communications* thanks Wenwei Liu, Augusto Martins, Ibrahim Tanriover, and You Zhou for their contribution to the peer review of this work. A peer review file is available.

Reprints and permissions information is available at http://www.nature.com/reprints

Publisher's note Springer Nature remains neutral with regard to jurisdictional claims in published maps and institutional affiliations.

Open Access This article is licensed under a Creative Commons Attribution-NonCommercial-NoDerivatives 4.0 International License, which permits any non-commercial use, sharing, distribution and reproduction in any medium or format, as long as you give appropriate credit to the original author(s) and the source, provide a link to the Creative Commons licence, and indicate if you modified the licensed material. You do not have permission under this licence to share adapted material derived from this article or parts of it. The images or other third party material in this article are included in the article's Creative Commons licence, unless indicated otherwise in a credit line to the material. If material is not included in the article's Creative Commons licence and your intended use is not permitted by statutory regulation or exceeds the permitted use, you will need to obtain permission directly from the copyright holder. To view a copy of this licence, visit http://creativecommons.org/licenses/by-nc-nd/4.0/.

© The Author(s) 2025